

# Building High-Density Au–Ag Islands on Au Nanocrystals by Partial Surface Passivation

Qikui Fan, Kai Liu, Ji Feng, Fumin Wang, Zhaojun Liu, Moxuan Liu, Yadong Yin, and Chuanbo Gao\*

As an advanced level of control in colloidal synthesis, it is highly desirable to create secondary structures of nanocrystals in a controllable manner for collective properties. Of particular interest is the generation of nanoislands of plasmonic metals (Ag and Au) at a high density around their pre-existing primary nanocrystals, which may produce abundant hotspots for surface-enhanced Raman scattering (SERS). Often such secondary structures are difficult to be achieved by direct crystal growth because a conformal growth is favorable due to the lattice match of these metals. Here, this challenge is overcome by developing a partial surface passivation strategy which can effectively shift the crystal growth mode from the “Frank–van der Merwe” mode to the “Volmer–Weber” mode, giving rise to nanoislands as a secondary structure on Au nanocrystals. The key to this strategy is the modification of the Au surface with Ag and subsequent adsorption of iodide at the Ag sites. Further deposition of Au on the modified surface leads to the formation of well-defined Au–Ag alloy islands of a high density on Au nanocrystals, which exhibit excellent SERS activity. This partial surface passivation strategy is fundamentally important and may inspire further endeavors in pursuit of novel secondary nanostructures and intriguing properties.

to tune the collective properties through their electronic, magnetic, and photonic interactions. This is especially important for applications based on the localized surface plasmon resonance (LSPR) of noble metal nanocrystals, such as surface-enhanced fluorescence and Raman scattering (SERS).<sup>[1–3]</sup> These surface-enhanced techniques largely rely on the creation of “hotspots,” i.e., spatially localized regions with extremely strong electromagnetic near fields, which is critically important to achieving boosted performance in these applications.<sup>[1,2]</sup> In addition to the creation of sharp tips<sup>[4–12]</sup> and rough surfaces<sup>[13–15]</sup> through morphologically controlled synthesis, hotspots can be constructed most effectively by creating nanogaps on or within metal nanostructures.<sup>[16–32]</sup> Although it is possible to produce such nanogaps by assembling pre-synthesized colloidal nanoparticles into secondary structures,<sup>[33–37]</sup> it would be more efficient, convenient, and reproducible to form the

## 1. Introduction

The development of colloidal synthesis has progressed to the point that it becomes routine to produce nanocrystals with well-controlled size, shape, composition, and surface properties. It is now highly desirable to design effective strategies to create secondary structures of nanocrystals in a highly controllable manner as it may provide enormous opportunities

secondary structures during their initial synthesis directly.

While it appears straightforward, it turns out to be highly challenging to construct secondary nanostructures on pre-existing Au or Ag nanocrystals, because the growth of Au or Ag on these nanocrystals usually produces conformal epitaxial overlayers, often referred to as the “Frank–van der Merwe” (FM) mode of the crystal growth, due to the tight lattice match in a monometallic or Au/Ag bimetallic system.<sup>[38–40]</sup> Although a “Volmer–Weber” (VW) mode is desired for the construction of nanoislands on these Au or Ag nanocrystals, it usually occurs in a bimetallic system with large lattice mismatch and thus poor wettability between the two components.<sup>[38–40]</sup> Recently, we found that the VW mode crystal growth could be achieved in metallic Au systems that possess very close or exactly the same lattice parameters by the surface capping of large polymeric ligands on the Au nanocrystals in synergy with a fast redox kinetics of the Au salt, leading to the growth of Au nanoislands.<sup>[15]</sup> While it opens many new opportunities, the binding strength of the conventional ligands may not be sufficiently strong for cases where a dense array of islands are desired, for example, for maximizing hotspots on pre-existing Au/Ag nanocrystals with high controllability.

In this work, we report a successful synthesis of high-density Au–Ag alloy nanoislands as secondary nanostructures on the surface of Au nanocrystals of an arbitrary choice, which is

Q. Fan, K. Liu, Z. Liu, M. Liu, Prof. C. Gao  
Frontier Institute of Science and Technology and State Key  
Laboratory of Multiphase Flow in Power Engineering  
Xi'an Jiaotong University  
Xi'an, Shaanxi 710054, China  
E-mail: gaochuanbo@mail.xjtu.edu.cn

J. Feng, Prof. Y. Yin  
Department of Chemistry  
University of California  
Riverside, CA 92521, USA

F. Wang  
School of Science  
Xi'an Jiaotong University  
Xi'an, Shaanxi 710049, China

 The ORCID identification number(s) for the author(s) of this article can be found under <https://doi.org/10.1002/adfm.201803199>.

DOI: 10.1002/adfm.201803199

enabled by strong adsorption of  $I^-$  on Ag-modified seed surface and thus surface heterogeneity for the seeded growth. This surface modification successfully shifts the crystal growth mode from FM to VW to produce Au–Ag alloy nanoislands of a controllable density on the surface of the Au nanocrystals. Therefore, it represents a simple, convenient and general method with excellent controllability. The resulting islands-on-Au nanocrystals show excellent SERS activity, thanks to the formation of high-density hotspots on the crystal surface, as demonstrated by the single-particle SERS with an enhancement factor of  $\approx 5 \times 10^6$ . We believe this study provides not only a convenient and general strategy for building secondary nanostructures on pre-existing metal nanocrystals but also further understandings on the growth behaviors of noble metal nanocrystals in pursuit of tailored nanostructures and properties.

## 2. Results and Discussion

As described in our previous work,<sup>[41,42]</sup> a robust seeded synthesis system of Au nanospheres (AuNSs) may include polyvinylpyrrolidone (PVP) as a surfactant,  $H AuCl_4$  as an Au source, KI as a coordinating ligand to the Au salt, and ascorbic acid (AA) as a reducing agent, which enables continuous FM mode crystal growth of the Au seeds to produce AuNSs of a broadly tunable size. Here,  $AgNO_3$  is introduced into this seeded growth system, which proves to be effective in shifting the crystal growth mode from FM to VW, and hence the product from conformal nanospheres to Au–Ag alloy nanoislands of a high density on the surface of the Au seeds (islands-on-AuNSs, containing  $\approx 7\%$  Ag). The growth of the nanoislands on the spherical Au seeds (size,  $\approx 50$  nm) can be confirmed by the transmission electron microscopy (TEM) and the high-angle

annular dark-field scanning transmission electron microscopy (HAADF-STEM) images (Figure 1a–e). Initially, the AuNSs possessed a smooth surface before the seeded growth (Figure 1a). After the seeded growth in the presence of  $AgNO_3$ , nanoislands were formed on the Au surface, instead of a smooth conformal layer. Sparse nanoislands emerged on the Au surface at a low concentration of  $H AuCl_4$ , which represents an intermediate formed at an early stage of the nanoislands growth (Figure 1b). With increasing concentrations of  $H AuCl_4$ , Au nanoislands were formed with a continuously increasing density, which eventually evolved into a fully fluffy nanostructure,  $\approx 65$  nm in size, after the extensive growth (Figure 1c–e). The electron microscopy images further reveal a high morphological yield of the islands-on-AuNSs, confirming the robustness of this synthesis.

The growth of the Au–Ag alloy nanoislands on the surface of the AuNSs has imposed strong influence on their optical property, as evidenced by the UV–vis spectroscopy (Figure 1f). The AuNSs with a smooth surface display a pronounced dipole-mode LSPR band at  $\approx 531$  nm of the wavelength. During the growth of the nanoislands, the LSPR band becomes broadening and continuously shifts to the long wavelengths, eventually to  $\approx 588$  nm at a high density of the nanoislands. To understand the nanoislands-induced change in the optical property, we conducted theoretical simulations of three models surrounded by water, i.e., AuNSs (50 nm) with a smooth surface, and islands-on-AuNSs with a low (400 on the Au surface) and high density (600 on the Au surface) of the nanoislands, by the finite-difference time-domain (FDTD) method (Figure 2). The results suggest that an increased density of the nanoislands results in a continuous redshift of the extinction band (Figure 2a), in agreement with the experimental UV–vis spectroscopy results. Compared with the AuNSs, the islands-on-AuNSs show much

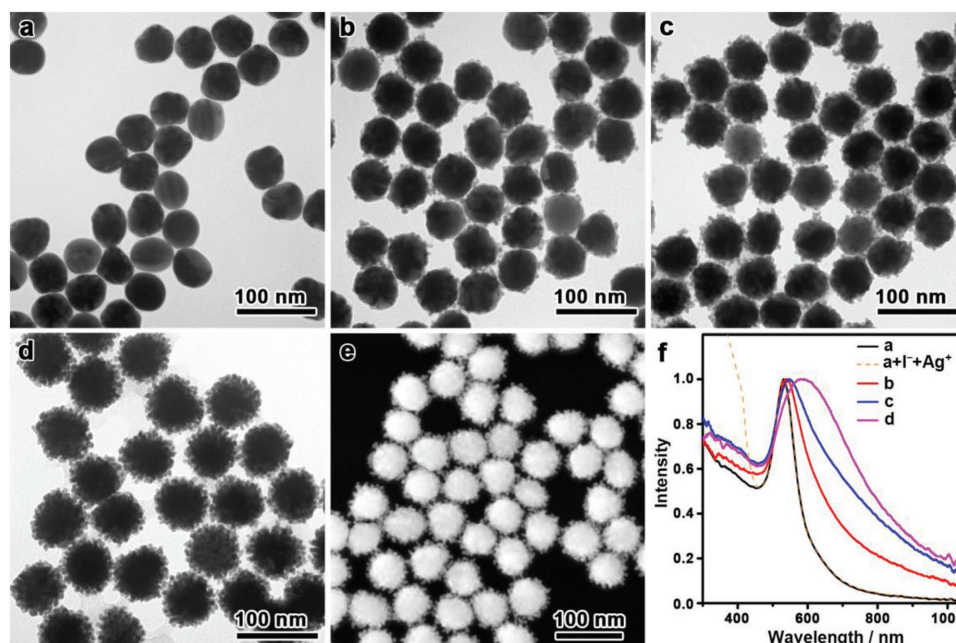


**Figure 1.** a) TEM images of the AuNSs. b–d) TEM images of the islands-on-AuNSs with varying densities of the nanoislands by changing the concentration of  $H AuCl_4$ . e) HAADF-STEM image of the islands-on-AuNSs as shown in (d). f) UV–vis extinction spectra of the AuNSs and the islands-on-AuNSs, corresponding to (a–d). Also included is the spectrum recorded after the addition of KI and  $AgNO_3$  to the sol of the AuNSs (dashed line).

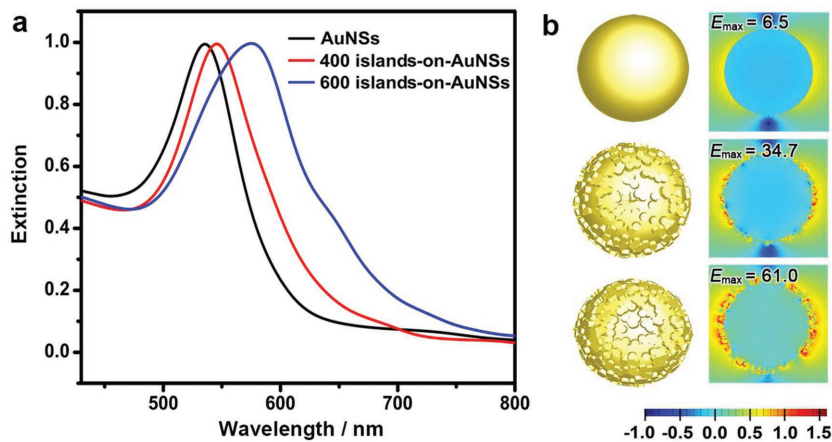


**Figure 2.** Simulated optical property of the islands-on-AuNSs. a) Extinction profiles of the AuNSs and the islands-on-AuNSs with different densities of the nanoislands. b) Simulated distributions of the electromagnetic field at the proximity of the AuNSs and the islands-on-AuNSs under the excitation of a 633 nm plane wave. The colors represent  $\log(|E|/|E_0|)$ , where  $E$  and  $E_0$  are the local and incident electromagnetic fields, respectively. Inset: maximum intensity ( $|E|/|E_0|$ ) of the electromagnetic field ( $E_{\max}$ ).

focused electromagnetic field at the proximity of the nanoislands, indicative of the formation of the hotspots (Figure 2b). As the density of the nanoislands increases, the intensity of the local electromagnetic fields gets stronger, accompanying a significant expansion of the hotspots over the entire surface of the nanosphere, which promises enhanced activity in SERS. The localization of the electromagnetic fields also suggests an enrichment of the charges at the nanoislands and therefore the weakened restoring force in their oscillation, which explains the redshift of the resonance relative to that of the AuNSs (Figures 1f and 2a). It is worth noting that the nanoislands can be excited by a much wider range of the wavelength (Figure S1, Supporting Information), which accounts for the broadening of the LSPR band in the UV–vis extinction spectrum of the islands-on-AuNSs.

Further investigations were conducted to understand the mechanism for the shift of the crystal growth mode in the synthesis of the nanoislands. In a control experiment, only conformal AuNSs with a smooth surface could be obtained in the absence of  $\text{AgNO}_3$  and KI (Figure S2, Supporting Information). With increasing concentrations of  $\text{AgNO}_3$  and KI, the nanoislands become continuously denser on the surface of the AuNSs, which suggests that  $\text{AgNO}_3$  and KI play a critical role in the transition of the crystal growth mode from FM to VW to afford the islands-on-AuNSs (Figure S2, Supporting Information). Upon mixing  $\text{AgNO}_3$  and KI, AgI nanoparticles form first, as evidenced by the UV–vis absorption at  $\approx 400$  nm (Figure 1f), which may nucleate at the surface of the AuNSs for partial passivation to suppress the conformal crystal growth.<sup>[43–45]</sup> To examine this possibility, we carried out a control experiment by allowing the formation of the AgI nanoparticles prior to the addition of the Au seeds. It produces virtually the same islands-on-AuNSs despite a lack of conjugation between the AuNSs and the AgI nanoparticles (Figure S3, Supporting Information), which rules out this option. It is reasonable that the partial surface passivation is still valid for the nanoislands growth, which, however, is through the Ag–I bonding at the

atomic scale, instead of the coverage by AgI nanoparticles (Figure 3). In brief, the pre-formed AgI nanoparticles are reduced to elemental Ag, which modifies the surface of the AuNSs. The iodide ions are thus released and subsequently adsorbed at the Ag sites to form strong Ag–I bonds. The surface bonds must be cleaved for a conformal FM mode crystal growth, which becomes energetically unfavorable in this synthesis due to the particular high Ag–I binding energy. Therefore, the metal deposition and convenient migration to these sites are suppressed, which leads to the formation of abundant nanoislands as secondary structures on the surface of the AuNSs. It is worth noting that the formation of the nanoislands relies on appropriate concentrations of  $\text{AgNO}_3$  and KI in this synthesis. When their concentrations become too high, the deposition rate of the Au atoms is much decreased due to the complexation of  $\text{HAuCl}_4$  with  $\text{I}^-$ , which leads to

a conformal FM mode crystal growth, producing AuNSs with a smooth surface (Figure S2, Supporting Information). In addition, a variation in the concentration of  $\text{AgNO}_3$  may also affect the curvature of the nanoislands, which could be attributed to a change in the surface passivation of the nanocrystals and thus the kinetics in the crystal growth (Figure S4, Supporting Information).

To verify this mechanism, we carried out elemental analysis of the islands-on-AuNSs by the core-level X-ray photoelectron spectroscopy (XPS, Figure 4). Prior to the analysis, the islands-on-AuNSs were treated with methylamine once and washed thoroughly with water to ensure the removal of the remaining AgI nanoparticles. The survey spectrum suggests that Ag, Au, and I elements remain on the islands-on-AuNSs (Figure 4a). Because the assignment of the oxidation states of Ag by XPS is of considerable ambiguity, the high-resolution spectrum was taken at the Auger region (Figure 4b), which clearly shows MVV peaks at 351.6 and 357.8 eV of the kinetic energy, corresponding to the elemental Ag(0). No additional peaks could be observed at  $\approx 351.2$  and 356.6 eV, which confirm the absence of Ag(I) species in the islands-on-AuNSs. The core-level Au 4f spectrum shows two spin–orbit split components at 83.5 and 87.1 eV of the binding energy, which can be ascribed to the elemental Au(0) (Figure 4c). Therefore, both Ag and Au are reduced to

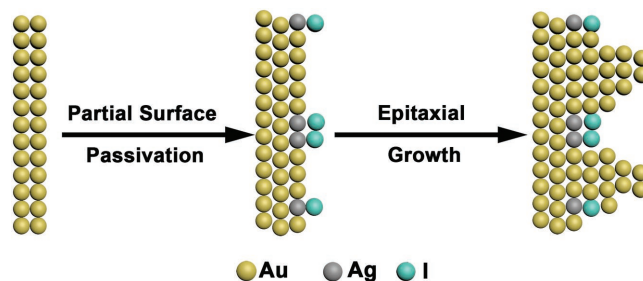


**Figure 3.** A cartoon illustrating the formation of the islands-on-Au nanostructures.

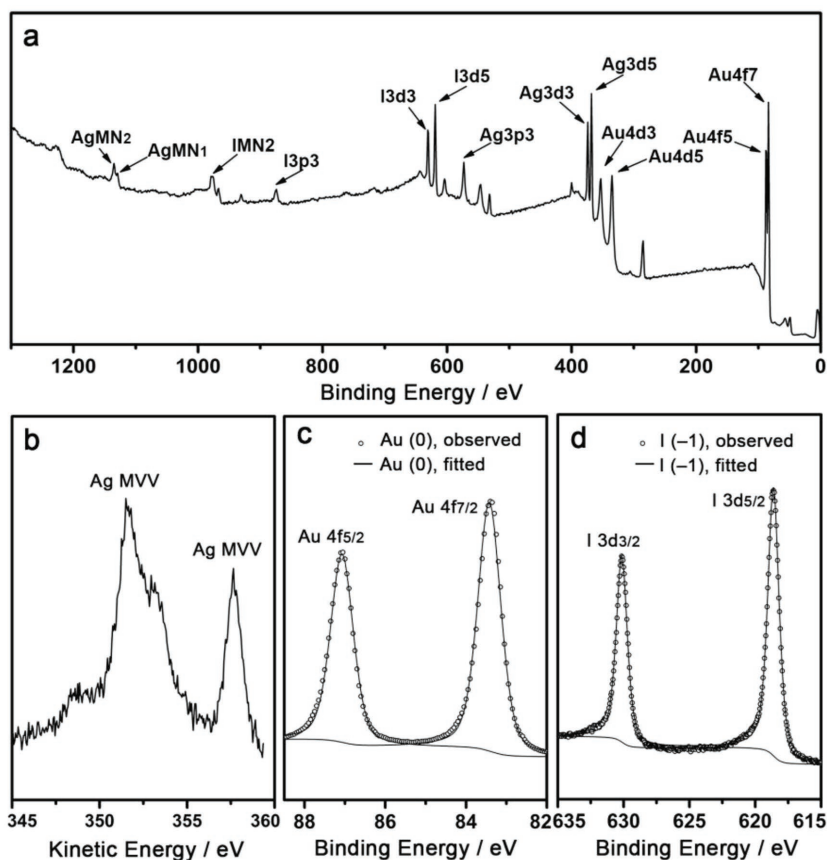


**Figure 4.** Elemental analysis of the islands-on-AuNSs. a) Survey of the XPS spectrum; b) Auger spectrum of Ag; c, d) Core-level XPS spectra of Au and I, respectively.

form the bimetallic alloy islands-on-AuNSs. The I 3d spectrum can be fitted by the  $3d_{5/2}$  and  $3d_{3/2}$  components at 618.6 and 630.2 eV, respectively, indicating the presence of the  $I^-$  species (Figure 4d). It confirms that  $I^-$  can strongly adsorb on the metal surface, which is responsible for the effective surface passivation, in line with our hypothesis. It is worth noting that the partial surface passivation can also be achieved by Ag–Cl and Ag–Br interactions in a similar manner, which turns out to be effective in producing nanoislands structures and further verifies the generality of this strategy (Figure S5, Supporting Information).

The distributions of the elements (Au, Ag, and I) in the islands-on-AuNSs were further examined by the energy dispersive X-ray spectroscopy (EDS) elemental mapping (Figure 5a) and a line elemental scan (Figure 5b, c). At the edges of the nanospheres (corresponding to the nanoislands), the distributions of Au and Ag well overlap, which confirm the effective Au–Ag alloying in the nanoislands. The local Au/Ag ratios could be estimated to be 2–4 in the Au–Ag alloy nanoislands, according to the line scan (Figure 5c). The formation of the Au–Ag alloy enables high stability of the nanoislands against chemical etching (Figure S6, Supporting Information). It is clear that both Ag and I are distributed at the edges (nanoislands) of the nanospheres following a similar trend in the distribution profile (Figure 5c), which further validates our hypothesis on the Ag–I surface passivation for the controlled growth of high-density Au–Ag alloy nanoislands.

This strategy to synthesize Au–Ag alloy nanoislands on the Au surface relies on the modification of the Au surface with Ag and the subsequent formation of the Ag–I bonds before the seeded growth, which is independent of the morphology of the Au nanocrystals, and therefore is widely applicable. To demonstrate it, we successfully synthesized nanoislands on Ag@Au nanoplates (NPs) and Au nanorods (NRs) by following a similar procedure (Figure 6, synthesis see Supporting Information). In both syntheses, the crystal growth mode has shifted from the FM to the VW mode, which leads to a fluffy surface with a high roughness, and promises excellent activity in SERS applications. The density of the nanoislands can also be effectively tuned by the concentration of  $HAuCl_4$  in this synthesis, further confirming the versatility of the current strategy.

As applications such as SERS require a clean surface for enhanced accessibility of the hotspots by the analytes,<sup>[46]</sup> the iodide as a strong capping agent should be effectively removed from the islands-on-Au nanocrystals prior to the use, which can be achieved experimentally by washing the nanocrystals repetitively with methylamine (Figure 7). Methylamine is believed to etch and complex with Ag, and thus eliminate the remaining AgI nanoparticles as well as the surface Ag–I species.<sup>[16]</sup> The TEM images clearly indicate the removal of AgI nanoparticles by the etching process (Figure 7a, b). The EDS analysis further unambiguously confirms the effectiveness of this treatment in the

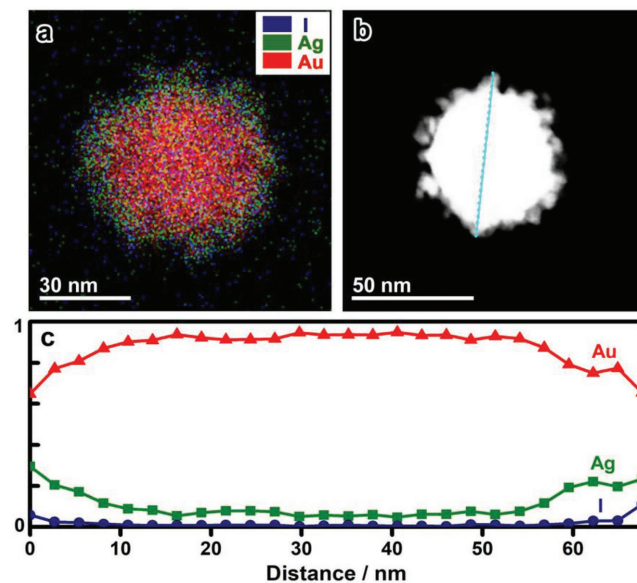


**Figure 5.** Elemental analysis of the islands-on-AuNSs. a) EDS elemental mapping of an individual islands-on-AuNS. b, c) Distributions of Au, Ag, and I along a line as indicated in the dark-field image.

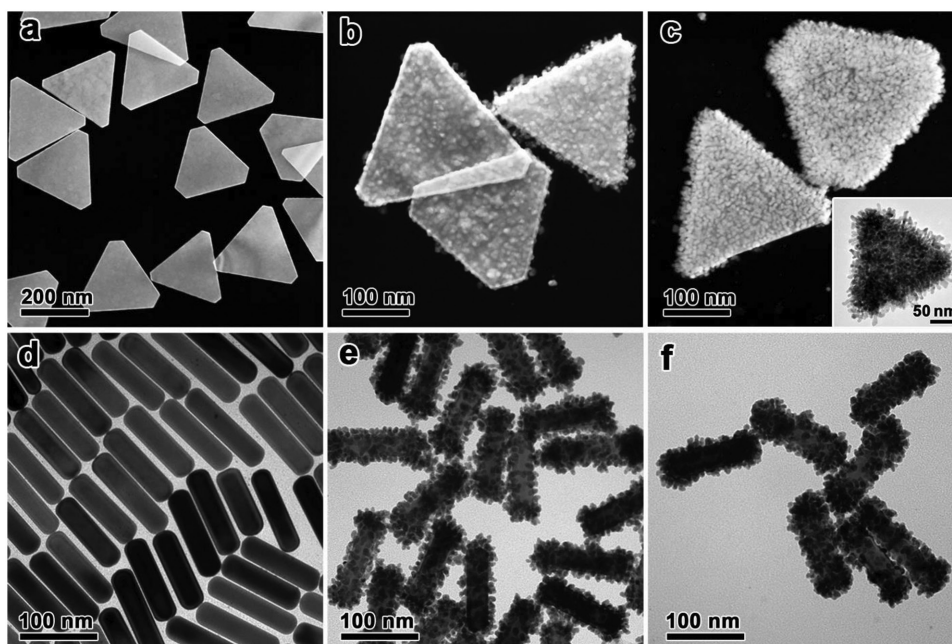


**Figure 6.** Various islands-on-Au nanostructures. a–c) STEM images of the Ag@AuNPs and the island-on-Ag@AuNPs with different density of the nanoislands, respectively. Inset of (c), TEM image of a single island-on-Ag@AuNP. d–f) TEM images of the AuNRs and the islands-on-AuNRs with a low and high density of the nanoislands, respectively.

surface cleaning (Figure 7c). The pristine islands-on-AuNSs showed characteristic X-ray signals from Au, Ag, and I. After cleaning with methylamine for seven times, the signals from I disappeared, while those from Au and Ag remained intact.

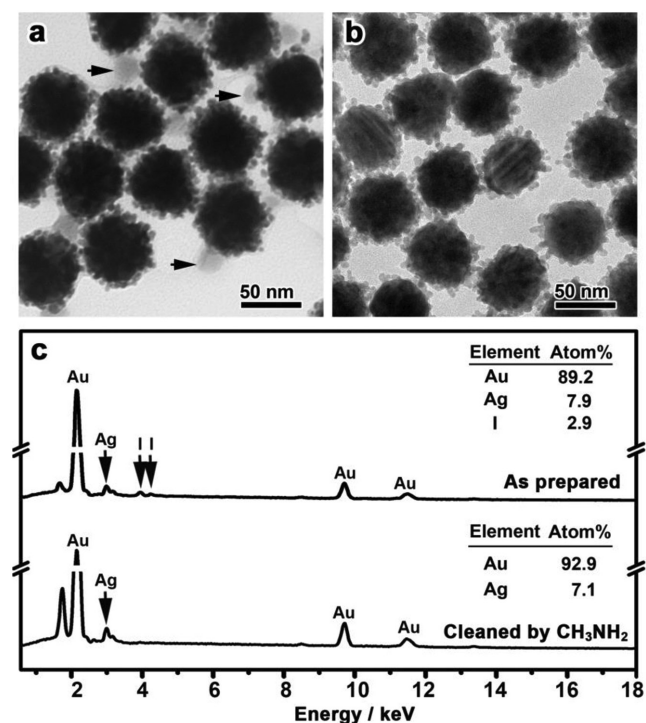


**Figure 7.** a, b) TEM images of the islands-on-AuNSs before and after the removal of the iodide, respectively. Arrows indicate AgI nanoparticles. c) EDS of the islands-on-AuNSs before and after the removal of the iodide.

Approximately, the islands-on-AuNSs contain 7.1% of Ag due to the effective co-reduction and alloying of Au and Ag during the nanoislands growth.

We experimentally examined the SERS activity of the islands-on-Au nanocrystals by benchmarking against the conventional AuNSs or AuNPs of a similar size (Figure 8 and Table S1, Supporting Information). Substrates were prepared by drying island-on-AuNSs and AuNSs of the same concentration and volume on separate silicon wafers followed by deposition of a known amount of crystal violet as a model analyte. At 633 nm irradiation, all the nanoparticles were excited when they assembled at the substrates (Figure S7, Supporting Information). Relatively large areas with consistent Raman intensity were obtained from these substrates (Figure S8, Supporting Information). When the density of the nanoislands was increasing, strong and well-resolved Raman vibrational peaks could be obtained with increasing intensities (Figure 8a, b), in good agreement of the near-field enhancement simulated by the FDTD method (Figure 2b). The intensity of the Raman signals obtained from the islands-on-AuNSs was enhanced by one order of magnitude relative to that of the AuNSs with a smooth surface. The excellent enhancement further enables sensitive detection of the analyte on a single particle basis, which was demonstrated by the islands-on-AuNPs in our experiments (Figure 8c, d). A single particle was located on the silicon substrate by the scanning electron microscopy (SEM) and optical microscopy imaging. While no apparent Raman signals could be detected from a single AuNP with a smooth surface, intense Raman signals have been observed from a single islands-on-AuNP with high-density nanoislands. The enhancement factor offered by the islands-on-AuNP was estimated to be  $\approx 5 \times 10^6$  based on the Raman signal at  $1613 \text{ cm}^{-1}$  (Supporting Information). It confirms the successful creation of inherent hotspots on the Au

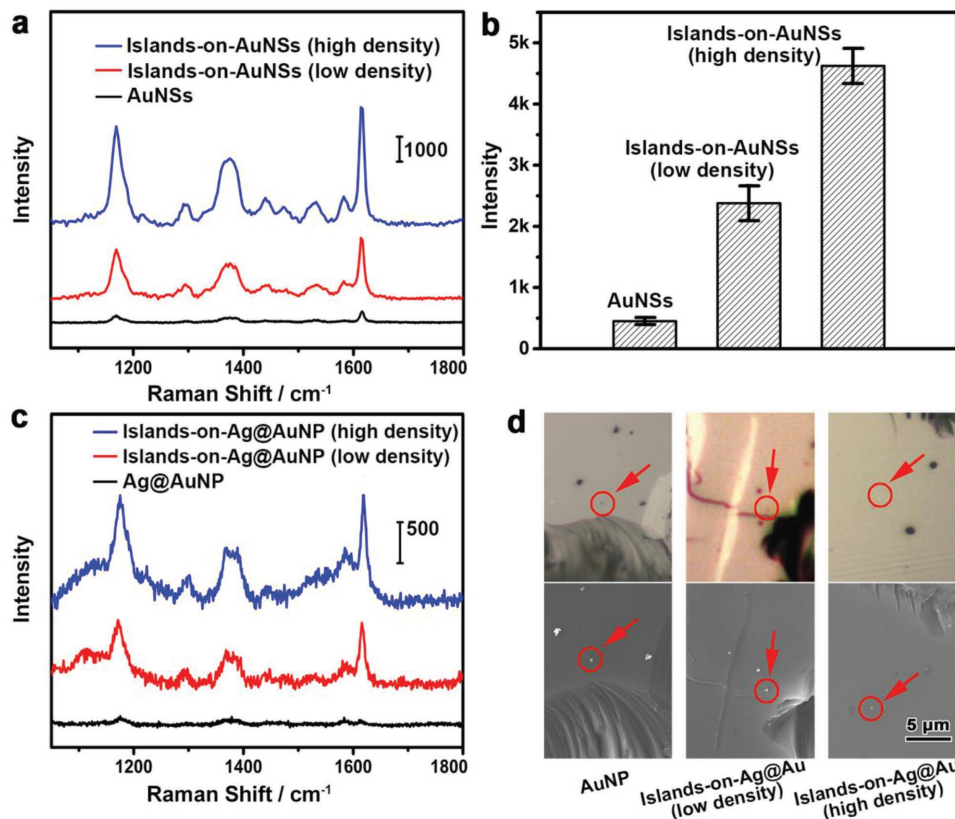


**Figure 8.** SERS activities of the islands-on-Au nanocrystals. a) Raman spectra of crystal violet from the islands-on-AuNSs with different density of the nanoislands, in comparison with that from the AuNSs. b) A comparison of the Raman intensities at  $1613\text{ cm}^{-1}$  as shown in (a). Error bars indicate the respective standard deviations obtained from more than seven parallel measurements. c) Raman spectra of crystal violet from a single particle of the islands-on-AuNP and with different densities of the nanoislands, as well as a bare AuNP. d) Corresponding single NPs subjected to the SERS analysis imaged by the SEM and optical microscope.

nanocrystals by the convenient nanoislands growth, the superior SERS activity of the resulting islands-on-Au nanocrystals, and their great potentials in single-particle SERS applications.

### 3. Conclusion

In summary, we have demonstrated a robust method for the synthesis of Au–Ag alloy nanoislands as secondary nanostructures on the surface of pre-existing Au nanocrystals, which allows effective fabrication of abundant inherent hotspots on the Au nanocrystals for plasmonic applications. The key to the synthesis is the modification of the Au surface with Ag and the subsequent adsorption of iodide ions at the Ag sites, which leads to partial surface passivation, and thus the shift of the crystal growth mode from the FM mode (layer-by-layer growth) to the VW mode (islands growth). The formation of the nanoislands significantly alters the optical property of the Au nanocrystals and enables excellent activity in SERS applications. We believe this study provides a convenient and general strategy for constructing secondary nanostructures on the surface of pre-existing Au nanocrystals on demand for significantly enhanced activity in a broad range of plasmonic applications and may be extendable to many other noble metal systems for intriguing structures and properties.

### 4. Experimental Section

**Synthesis of Nanoislands on Au Nanospheres:** In a typical synthesis,  $500\text{ }\mu\text{L}$  of AuNSs ( $\approx 50\text{ nm}$ ,  $0.89\text{ g L}^{-1}$ ,  $1.2 \times 10^{-9}\text{ M}$ , synthesis see Supporting Information),  $1\text{ mL}$  of PVP (0.05 wt%, Mw 10000),  $400\text{ }\mu\text{L}$  of  $\text{AgNO}_3$  ( $10 \times 10^{-3}\text{ M}$ ), and  $200\text{ }\mu\text{L}$  of KI ( $20 \times 10^{-3}\text{ M}$ ) were added in order in  $10\text{ mL}$  of  $\text{H}_2\text{O}$  at room temperature. After stirring for 2 min,  $90\text{ }\mu\text{L}$  of  $\text{HAuCl}_4$  ( $25 \times 10^{-3}\text{ M}$ ) and  $5\text{ mL}$  of L-AA ( $20 \times 10^{-3}\text{ M}$ ) were injected into the above solution. The reaction was allowed to proceed for 3 min. The resulting islands-on-AuNSs were collected by centrifugation, washed with  $\text{H}_2\text{O}$ , and redispersed in  $20\text{ mL}$  of  $\text{H}_2\text{O}$ . The islands-on-AuNSs were washed with methylamine for seven times prior to the SERS analysis.

**SERS Activity Measurements:** Islands-on-AuNSs ( $25\text{ }\mu\text{L}$ ) were deposited on a clean silicon wafer ( $8\text{ mm} \times 8\text{ mm}$ ). Then,  $25\text{ }\mu\text{L}$  of crystal violet ( $10^{-6}\text{ M}$ ) was dropped and dried on it and washed three times with  $\text{H}_2\text{O}$ . Raman spectra were recorded with a  $633\text{ nm}$  He–Ne laser line at room temperature. The size of the laser spot was  $0.86\text{ }\mu\text{m}$  under a  $100\times$  objective, the power density was  $51.7\text{ kW}\cdot\text{cm}^{-2}$  at the substrate, and the signal acquisition time was 1 s. In a single-particle SERS analysis, a highly diluted solution of the islands-on-AuNPs was deposited on a clean silicon wafer ( $8\text{ mm} \times 8\text{ mm}$ ), followed by drying  $25\text{ }\mu\text{L}$  of crystal violet ( $10^{-6}\text{ M}$ ) on it and subsequent washing three times with  $\text{H}_2\text{O}$ . Raman spectra were recorded from a single NP. The power density was  $51.7\text{ kW}\cdot\text{cm}^{-2}$  at the substrate, and the signal acquisition time was 10 s.

**Finite-Difference Time-Domain Simulation:** The three-dimensional FDTD simulation was used to calculate the electromagnetic field distributions and extinction efficiencies of the islands-on-AuNSs. A single islands-on-AuNS was modeled, which was irradiated by a plane wave at different wavelengths. The surrounding medium of the model

structure was set to be H<sub>2</sub>O. All simulations were performed with numerical FDTD Solutions.

**Characterizations:** TEM was performed on an HT7700 operated at an acceleration voltage of 100 kV. HAADF-STEM and elemental mapping were performed on a JEM-F200-TEM operated at 200 kV. SEM and EDS were taken on a field-emission FEI Quanta FEG 250 microscope operated at an acceleration voltage of 20 kV. UV-vis spectra ( $\lambda$ : 300–1000 nm) were measured on an Ocean Optics HR2000+ES UV-vis-NIR spectrophotometer with a DH-2000-Bal light source. XPS measurements were performed on a Thermo Fisher scientific ESCALAB Xi+ with monochromatic Al K $\alpha$  radiation. The Au 4f peaks were fitted by 4f<sub>7/2</sub> and 4f<sub>5/2</sub> doublets with a binding energy difference of 3.65 eV and an area ratio of 4/3. The I 3d peaks were fitted by 3d<sub>5/2</sub> and 3d<sub>3/2</sub> doublets with a binding energy difference of 11.52 eV and an area ratio of 3/2. For each set of the doublet peaks, the full-width at half maximum was set to be the same. Raman spectra were collected using a LabRAM HR800 confocal Raman spectrophotometer equipped with a 633 nm He–Ne laser.

## Supporting Information

Supporting Information is available from the Wiley Online Library or from the author.

## Acknowledgements

C.G. acknowledges the support from the National Natural Science Foundation of China (21671156 and 21301138) and the Tang Scholar Program from Cyrus Tang Foundation. Y.Y. acknowledges the support from the U.S. National Science Foundation (CHE-1308587). The authors are grateful to the Instrument Analysis Center of Xi'an Jiaotong University (XJTU) for access to the TEM and XPS, and Prof. Liqing Huang at School of Science (XJTU) for help with FDTD simulations. Acknowledgment is also made to the Donors of the American Chemical Society Petroleum Research Fund for partial support of this research.

## Conflict of Interest

The authors declare no conflict of interest.

## Keywords

epitaxial growth, island growth, noble metal nanocrystals, partial surface passivation, surface plasmon resonance

Received: May 9, 2018  
Revised: July 11, 2018  
Published online:

- [1] C. L. Haynes, A. D. McFarland, R. P. V. Duyne, *Anal. Chem.* **2005**, *77*, 338 A.
- [2] S. Schlucker, *Angew. Chem. Int. Ed.* **2014**, *53*, 4756.
- [3] R. Bardhan, S. Lal, A. Joshi, N. J. Halas, *Acc. Chem. Res.* **2011**, *44*, 936.
- [4] C. G. Khoury, T. Vo-Dinh, *J. Phys. Chem. C* **2008**, *112*, 18849.
- [5] M. J. Mulvihill, X. Y. Ling, J. Henzie, P. Yang, *J. Am. Chem. Soc.* **2009**, *132*, 268.
- [6] C. J. DeSantis, A. A. Peverly, D. G. Peters, S. E. Skrabalak, *Nano Lett.* **2011**, *11*, 2164.
- [7] P. Aldeanueva-Potel, E. Carbó-Argibay, N. Pazos Pérez, S. Barbosa, I. Pastoriza-Santos, R. A. Alvarez Puebla, L. M. Liz-Marzán, *ChemPhysChem* **2012**, *13*, 2561.
- [8] S. Pedireddy, A. Li, M. Bosman, I. Y. Phang, S. Li, X. Y. Ling, *J. Phys. Chem. C* **2013**, *117*, 16640.
- [9] Z. Liu, Z. Yang, B. Peng, C. Cao, C. Zhang, H. You, Q. Xiong, Z. Li, J. Fang, *Adv. Mater.* **2014**, *26*, 2431.
- [10] J. Morla-Folch, L. Guerrini, N. Pazos Pérez, R. Arenal, R. A. Alvarez Puebla, *ACS Photonics* **2014**, *1*, 1237.
- [11] R. G. Weiner, S. E. Skrabalak, *Angew. Chem. Int. Ed.* **2015**, *54*, 1181.
- [12] L. Zhang, X. Sha, Q. Fan, L. Han, Y. Yin, C. Gao, *Nanoscale* **2017**, *277*, 1078.
- [13] H. Wang, N. J. Halas, *Adv. Mater.* **2008**, *20*, 820.
- [14] H. You, Y. Ji, L. Wang, S. Yang, Z. Yang, J. Fang, X. Song, B. Ding, *J. Mater. Chem.* **2012**, *22*, 1998.
- [15] G. Wang, Y. Liu, C. Gao, L. Guo, M. Chi, K. Ijiro, M. Maeda, Y. Yin, *Chem* **2017**, *3*, 678.
- [16] L. Zhang, T. Liu, K. Liu, L. Han, Y. Yin, C. Gao, *Nano Lett.* **2015**, *15*, 4448.
- [17] M. Yang, R. n. Alvarez-Puebla, H.-S. Kim, P. Aldeanueva-Potel, L. M. Liz-Marzán, N. A. Kotov, *Nano Lett.* **2010**, *10*, 4013.
- [18] J. Song, B. Duan, C. Wang, J. Zhou, L. Pu, Z. Fang, P. Wang, T. T. Lim, H. Duan, *J. Am. Chem. Soc.* **2014**, *136*, 6838.
- [19] J. W. Oh, D. K. Lim, G. H. Kim, Y. D. Suh, J. M. Nam, *J. Am. Chem. Soc.* **2014**, *136*, 14052.
- [20] D. K. Lim, K. S. Jeon, J. H. Hwang, H. Kim, S. Kwon, Y. D. Suh, J. M. Nam, *Nat. Nanotechnol.* **2011**, *6*, 452.
- [21] Y. Jin, X. Gao, *Nat. Nanotechnol.* **2009**, *4*, 571.
- [22] C. Ayala-Orozco, J. G. Liu, M. W. Knight, Y. Wang, J. K. Day, P. Nordlander, N. J. Halas, *Nano Lett.* **2014**, *14*, 2926.
- [23] T. Zhang, F. Zhou, L. Hang, Y. Sun, D. Liu, H. Li, G. Liu, X. Lyu, C. Li, W. Cai, Y. Li, *J. Mater. Chem. C* **2017**, *5*, 11039.
- [24] T. Zhang, Y. Sun, L. Hang, H. Li, G. Liu, X. Zhang, X. Lyu, W. Cai, Y. Li, *ACS Appl. Mater. Interfaces* **2018**, *10*, 9792.
- [25] Q. Zhang, N. Large, P. Nordlander, H. Wang, *J. Phys. Chem. Lett.* **2014**, *5*, 370.
- [26] Y. Yan, A. I. Radu, W. Rao, H. Wang, G. Chen, K. Weber, D. Wang, D. Cialla-May, J. Popp, P. Schaaf, *Chem. Mater.* **2016**, *28*, 7673.
- [27] X. Wei, Q. Fan, H. Liu, Y. Bai, L. Zhang, H. Zheng, Y. Yin, C. Gao, *Nanoscale* **2016**, *8*, 15689.
- [28] D. Wang, P. Schaaf, *J. Mater. Chem.* **2012**, *22*, 5344.
- [29] C. Vidal, D. Wang, P. Schaaf, C. Hrelescu, T. A. Klar, *ACS Photonics* **2015**, *2*, 1436.
- [30] W. Rao, D. Wang, T. Kups, E. Baradács, B. Parditka, Z. Erdélyi, P. Schaaf, *ACS Appl. Mater. Interfaces* **2017**, *9*, 6273.
- [31] K. Liu, Y. Bai, L. Zhang, Z. Yang, Q. Fan, H. Zheng, Y. Yin, C. Gao, *Nano Lett.* **2016**, *16*, 3675.
- [32] M. K. Khristosov, L. Bloch, M. Burghammer, Y. Kauffmann, A. Katsman, B. Pokroy, *Nat. Commun.* **2015**, *6*, 8841.
- [33] X. Shen, L. Chen, D. Li, L. Zhu, H. Wang, C. Liu, Y. Wang, Q. Xiong, H. Chen, *ACS Nano* **2011**, *5*, 8426.
- [34] H. Wang, L. Chen, X. Shen, L. Zhu, J. He, H. Chen, *Angew. Chem. Int. Ed.* **2012**, *51*, 8021.
- [35] V. T. Cong, E. O. Ganbold, J. K. Saha, J. Jang, J. Min, J. Choo, S. Kim, N. W. Song, S. J. Son, S. B. Lee, S. W. Joo, *J. Am. Chem. Soc.* **2014**, *136*, 3833.
- [36] D. Iliu, F. Zhou, C. Li, T. Zhang, H. Zhang, W. Cai, Y. Li, *Angew. Chem. Int. Ed.* **2015**, *54*, 9596.
- [37] L. Zhang, Q. Fan, X. Sha, P. Zhong, J. Zhang, Y. Yin, C. Gao, *Chem. Sci.* **2017**, *8*, 6103.
- [38] S. E. Habas, H. Lee, V. Radmilovic, G. A. Somorjai, P. Yang, *Nat. Mater.* **2007**, *6*, 692.
- [39] F. R. Fan, D.-Y. Liu, Y.-F. Wu, S. Duan, Z.-X. Xie, Z.-Y. Jiang, Z.-Q. Tian, *J. Am. Chem. Soc.* **2008**, *130*, 6949.
- [40] K. D. Gilroy, A. Ruditskiy, H.-C. Peng, D. Qin, Y. Xia, *Chem. Rev.* **2016**, *116*, 10414.
- [41] C. Gao, J. Vuong, Q. Zhang, Y. Liu, Y. Yin, *Nanoscale* **2012**, *4*, 2875.
- [42] C. Gao, J. Goebel, Y. Yin, *J. Mater. Chem. C* **2013**, *1*, 3898.
- [43] Y. Sun, I. V. Jonathan J. Foley, S. Peng, Z. Li, S. K. Gray, *Nano Lett.* **2013**, *13*, 3958.
- [44] Y. Sun, *Natl. Sci. Rev.* **2015**, *2*, 329.
- [45] Y. Hu, Y. Liu, Z. Li, Y. Sun, *Adv. Funct. Mater.* **2014**, *24*, 2828.
- [46] Q. Fan, K. Liu, Z. Liu, H. Liu, L. Zhang, P. Zhong, C. Gao, *Part. Part. Syst. Character.* **2017**, *34*, 1700075.